ANALYZING PEACEFUL NUCLEAR EXPLOSION ARRIVAL CODAS FOR CRUSTAL PROPERTIES

Igor B. Morozov,[1] Hongyan Li,[2] Joel N. Duenow,[2] and Scott B. Smithson[2]

University of Saskatchewan;[1] University of Wyoming[2]

ABSTRACT

Coda amplitude decay of regional arrivals from Peaceful Nuclear Explosions (PNEs) could be used for characterization of crustal properties critical for seismic monitoring. In particular, as coda waves at 0.5–10 Hz are believed to consist predominantly of scattered shear waves, coda analysis could provide information about *Lg* attenuation and scattering from crustal heterogeneities. Digital recordings of 21 reversed PNEs—recorded by 200–400 three-component instruments within 0–3,000 km range in Northern Eurasia—enable coda amplitude measurements to provide valuable information for understanding *Lg* propagation in the region. In this project, we focus on the analysis of the spectral properties of *Lg*, crustal attenuation using the spectral and coda decay information extracted from the PNE records, and on modeling these characteristics.

Measurements of PNE phase amplitudes show that *Lg*/*Sn* and *Lg*/*Pg*$_{coda}$ RMS (root mean square) amplitude ratios significantly constrain variations of crustal structure. *Lg* coda *Q* computed using spectral ratio methods shows poor stability resulting from high noise and the narrow (1-5 Hz) frequency band; however, time-domain *Lg* coda *Q* estimates are stable and reflect variations of crustal structure. *Lg* arrivals are subdivided into shorter (~40-s) range-independent early parts, followed by longer codas with distinct exponential amplitude decay and with time durations increasing with range. Sediment thickness appears to be the most important factor affecting *Lg* coda attenuation, with lower *Lg* coda *Q* observed within sedimentary basins. We present a map of *Lg* coda *Q* values measured from PNE profiles, with potential areas of "*Lg* blockage" identified.

Our modeling effort targets realistic, three-component codas produced by a distant PNE source. Since three-dimensional (3-D) simulations are required for a correct description of short-period coda of PNE arrivals, we perform our modeling in 3-D by employing a single-scattering (Born) approximation. Reflectivity synthetics based on velocity models of different crustal and upper mantle properties are used as the Green's functions. The full seismic response is calculated using numerical integration in time and a 2D surface integral over uniformly distributed Monte-Carlo-sampled surface points. Coda *Q* values are measured on modeled records based on a range of intrinsic crustal *Q*'s to determine an empirical relationship of $Q_{coda}(Q_{crust})$. This relation, approximated as a power law, is further inverted to obtain Q_{crust} estimates for PNE data from the observed coda *Q* values.

Using the reflectivity synthetics in velocity models of greater crustal complexity leads to greater dependence of Q_{coda} on Q_{crust}. For the teleseismic *P* coda at 0.3 Hz, measurements of synthetic coda created using the Quartz-4 velocity model, gives $Q_{coda} = 16 \cdot Q_{crust}^{0.47}$ at 0.3 Hz and $Q_{coda} = 28 \cdot Q_{crust}^{0.43}$ at 0.7 Hz. The IASP-91 model, with a simpler 2-layer crust and mantle, gives a much weaker dependence, $Q_{coda} = 75 \cdot Q_{crust}^{0.06}$ at 0.3 Hz and $Q_{coda} = 75 \cdot Q_{crust}^{0.14}$ at 0.7 Hz. Our modeling suggests that the crust, and not the mantle, plays the most significant role in determining the $Q_{coda}(Q_{crust})$ dependence. Based on the empirical relationships above, we improve our previous measurements of the bulk crustal *Q* from Quartz PNE data, with the resulting Q_{crust} ranging from ~50 at 1.5 Hz to ~170 at 5 Hz.

Further research will include: (1) inversion of the amplitude and spectral decay parameters for variations in the regional crustal attenuation structure and correlation with tectonics; and (2) modeling of *Lg* propagation using an extension of the above technique. These studies should result in an improved model of the crustal properties and a comprehensive modeling capability that could be utilized for interpretation of both the average and the region-specific character of regional wave propagation in Northern Eurasia.

OBJECTIVE

Regional phases used in the Comprehensive Nuclear-Test-Ban Treaty (CTBT) monitoring (*Lg*, *Pg*, *Pn*, *Sn*) travel through the crust and the upper mantle, which are highly heterogeneous, and therefore amplitude and travel-time calibration of these phases requires understanding of their relation to the tectonic and geologic environment. This study focuses on

1) gathering of empirical data on amplitude and spectral ratio characteristics of regional phases from nuclear explosions of the Russian Deep Seismic sounding program, and

2) using numerical modeling to establish semi-empirical relationships between the *in situ* crustal properties and the observed wavefield characteristics. Among these characteristics, we are particularly interested in the quality factor, *Q*, describing attenuation of seismic waves.

RESEARCH ACCOMPLISHED

Of all the regional phases, the *Lg* is often the most prominent and robust regional phase in continental regions. It has been widely used to determine regional variation of crustal attenuation properties and to differentiate nuclear explosion from other sources. It depends on the rock type and the degree of heterogeneity and therefore could be correlated with the geological structure. *Lg* amplitude ratios, such as *Lg*/*Sn* (Sandvol, et al., 2001), *Pg*/*Lg* (Philips, et al., 2001), *Lg*/*Pg*$_{coda}$ (McNamara and Walter, 2001) are used for seismic source discrimination in different tectonic areas. Also, according to Walter, et al. (1995) and Koch (2002), *Lg* spectral ratios *Lg*(1–2Hz)/*Lg*(6–8Hz) or *Lg*$_{coda}$(1–2Hz)/*Lg*$_{coda}$(6–8Hz) provide good differentiation of nuclear explosions from earthquakes.
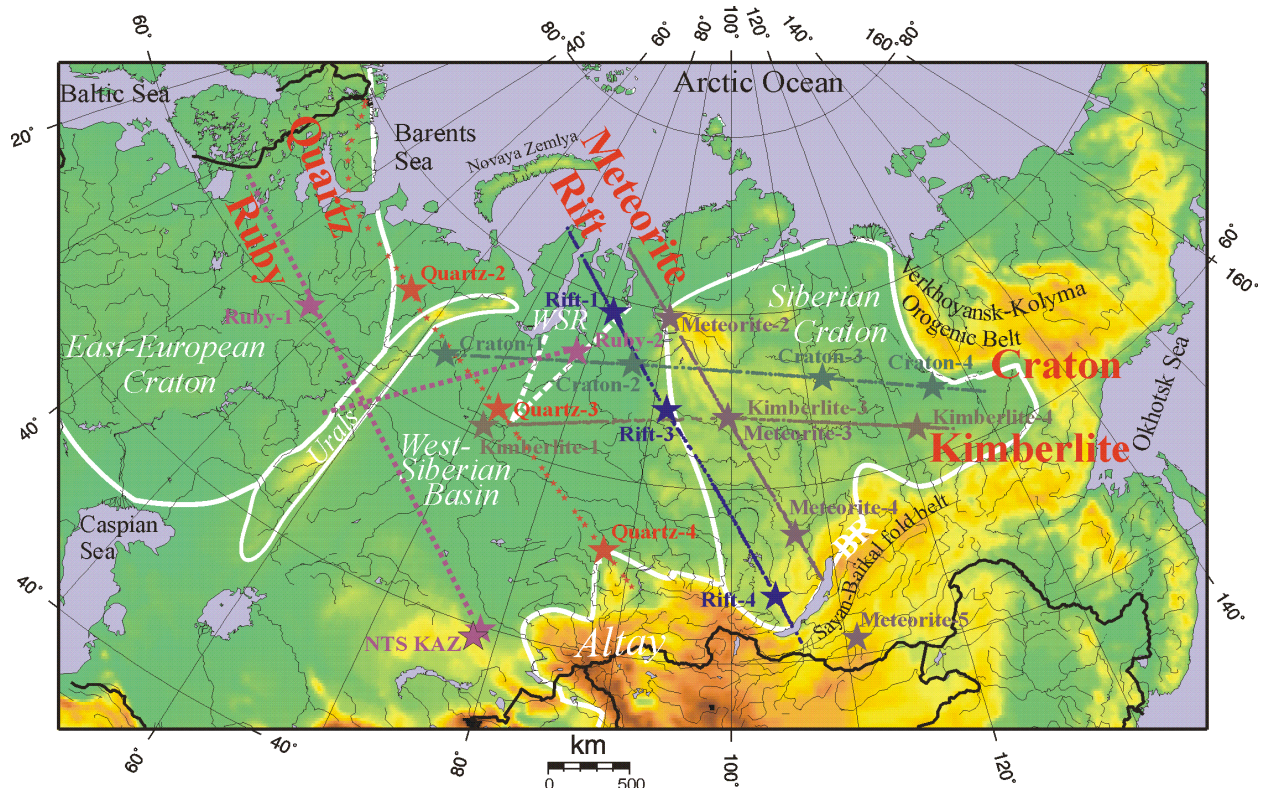

Figure 1. Location of PNE profiles and major tectonic boundaries. Large labeled stars indicate nuclear explosion locations, small stars are the chemical explosions. For profile Quartz, small dots show the chemical explosions; for other profiles - individual station locations. White lines show major tectonic features (WSR – West Siberian Rift, BR – Baikal Rift) and color represents the topography (Zonenshain, 1990).

Since at regional distances the *Lg* phase could be highly attenuated or even blocked with abrupt change in the crustal structure, it is crucial to gather information about *Lg* propagation across a variety of continental tectonic structures. However, Northern Eurasia is largely aseismic, and the regional recordings of natural sources are very limited. Also, path calibration of regional seismic phases is strongly dependent on the accuracy of hypo-central locations of calibration events (Saikia, 2001), and for earthquake data, especially for small events, this information is difficult to obtain. However, from the mid 1960s through late 1980s, Russian scientists acquired a network of dense, linear, long-range, three-component Deep Seismic Sounding (DSS) profiles using conventional and Peaceful Nuclear Explosions (PNEs) over almost all Northern Eurasia. At the University of Wyoming, we obtained records from seven PNE profiles and 19 PNEs of this program (Figure 1), and are analyzing them in order to extract ground truth and develop calibration techniques for CTBT monitoring.

Recent studies included: study the main factors that affect the *Lg* phase propagation characteristics, calibrate the detailed crustal structure in Northern Eurasia, study the attenuation properties quantitatively in Northern Eurasia, and try to find the better ways to differentiate nuclear explosions from earthquakes.

Correlation of the spectral ratios and *Lg* coda *Q* with the variations of the crustal structure. In order to study the effects of crustal structure on *Lg* phase propagation and calibrate the detailed in Northern Eurasia, we computed *Lg*/*Sn* and *Lg*/*Pg*$_{coda}$ RMS amplitude ratio. In addition, we measured the *Lg* coda *Q* to constrain crustal attenuation.

Figure 2 summarizes some of the attributes extracted from the records from PNE Craton-3. *Lg* coda *Q* was measured in a 120-s at 40 s after the picked *Lg* onset. The 40-s lag was chosen so that the early, steeper *Lg* coda was not included in the measurements. The frequency band was 1 to 2.5 Hz and the radial-component recordings were used in RMS estimates. A commonly used amplitude decay relation is:

$$A(f,t) = G(r)R(f)S(f)e^{-\pi ft/Q(f)},\qquad(1)$$

where, *G* is the geometric spreading factor, *R* and *S* are receiver and source response functions, respectively; *f* is the frequency; *t* is the travel time; and *Q* is the quality factor.

Logarithm of the amplitude ratio (1) at two times, t_1 and t_2, yields:

$$\log\left(A(f,t_1)/A(f,t_2)\right) = -\frac{\pi f(t_1 - t_2)}{Q(f)}\qquad(2)$$

Therefore, *Q* can be measured by 1) the change of the log*A*(*f*) slope with time; and 2) by measuring the log*A*(*t*) slope using band-pass filtered records. Thus the second (time-domain) method proves advantageous because of the greater stability of the resulting 1/*Q* values, and also because it allows using individual traces for estimation of *Lg* coda *Q*.

In comparing the resulting attributes (amplitude ratios and *Lg* coda *Q*) with geology, we are particularly interested in a possible correlation with the sedimentary basins. We profile the Craton across three major sedimentary basins: the Patom-Viluy Basin, the Tunguss Basin, and the West Siberian Basin (Figure 2a). The Patom-Viluy Basin is covered with very thick sediments (deeper than 15 km) and shallower Moho underneath; the sediments of Tunguss Basin are also deep (>10 km), but the velocity of the sediments is high (5.5 km/s), and the velocity of the lower crust is low (6.8 km/s). The sediment thickness in West-Siberian Basin reaches 8 km, and the velocities are low (3.5km/s). Note that there is a low-velocity zone identified within the uppermost mantle under the West-Siberian Basin (Pavlenkova, 1996). The heat flow is high (~70 mWm^{-2} in the West Siberian and Viluy Basins, and low at other locations (Pavlenkova, 1996).

Both the *Lg*/*Sn* and *Lg*/*Pg*$_{coda}$ amplitude ratios and particularly the *Lg* coda *Q* show correlation with the sedimentary basins crossed by the profile (Figure 2). Note that in Figure 2b, for the west branch, *Lg*/*Sn* increases from offset ~300km to ~600km, then decreases until offset ~800km (within the Tunguss Basin), then increases again until offset ~1,200km, then the ratio decreases quickly as the waves enter the West Siberian Basin. To the east, *Lg*/*Sn* increases slowly until offset ~600km, and then the ratio decreases rapidly, again within the Patum-Viluy basin. *Lg* coda *Q* shows similar behavior (Figure 2d). West of the PNE, the *Lg* coda *Q* first decreases until offsets of ~600km, then increases until to ~1,200km, and then decreases strongly within the West Siberian basin. To the east, *Lg* coda *Q* values stay nearly constant until offsets of ~600km, at Q≈450. For the western branch, the minimum Q value is ~300, and the maximum is ~400km. The scatter in *Lg* coda *Q* values west of the PNE is large, which may be a result

of the variations in the *Lg* amplitudes, as suggested by the increased scatter in the *Lg/Sn* and *Lg/Pg*$_{coda}$ RMS amplitude ratios.

The fact that the short-period *Lg* decreases in amplitude when recorded within a sedimentary basin and tends to rebound on its opposite side suggests that the *Lg* is attenuated by the sediments; yet significant *Lg* energy bypasses the basin through the mid- and lower-crust and "heal" the *Lg* amplitude afterwards. Increased *Lg* coda attenuation (lower *Q*) within the basins also corroborates this observation. It appears that the coda is formed primarily by *Lg* scattering near the receiver, within the upper crust of the basins. Indeed, localized anomalies of high-coda attenuation imply a source of strong scattering close to the receivers.

This interpretation of *Lg* coda *Q* is somewhat different from the model by Mitchell et al. (1997), in which they assumed that the coda could equally likely originate from *Lg*→*Lg* scattering on points distributed on system of ellipses having the source and receiver as their common foci. In their model, scattering amplitudes are assumed to be constant and independent on the scattering angles, and *Lg* coda 1/*Q* is formed as an areal average of Lg 1/*Q* values. However, scattering is likely to increase within the sedimentary basins, and to include other than *Lg*→*Lg*
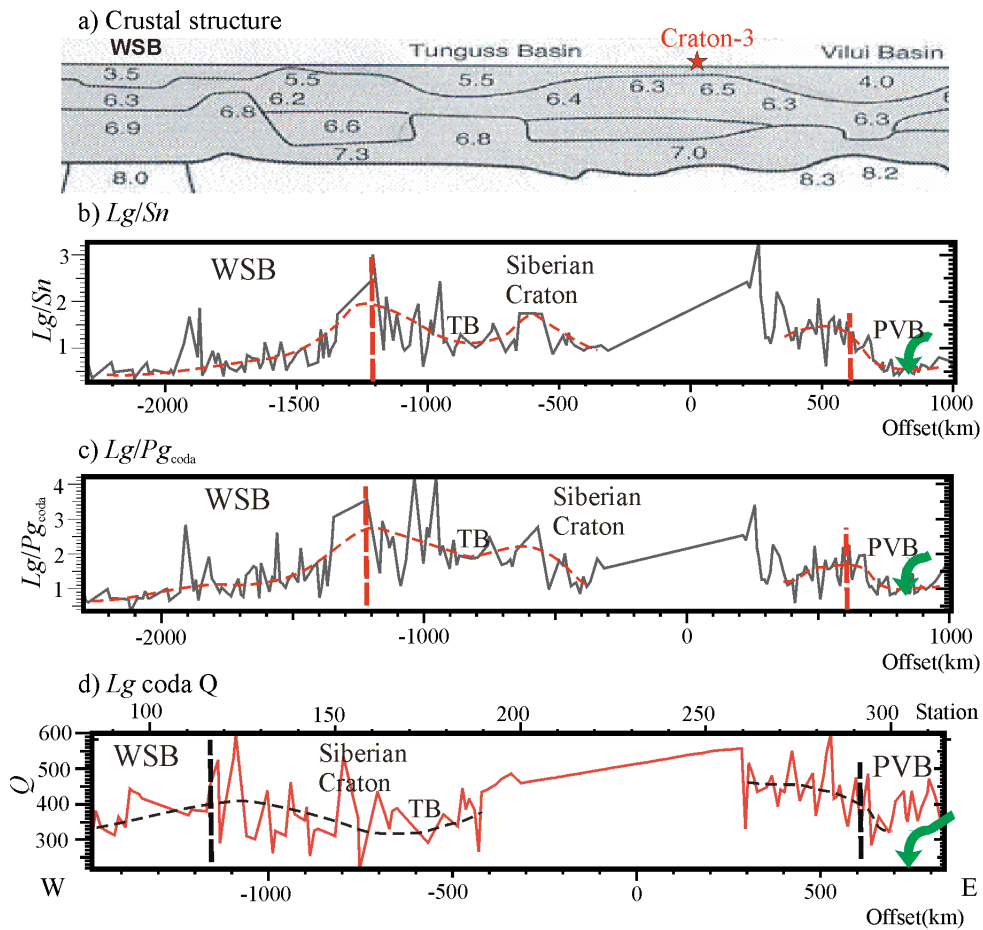

Figure 2. Regional phase attributes from PNE Craton-3: (a) crustal velocity model from Pavlenkova (1996), with P-wave velocity values labelled; (b) *Lg/Sn* RMS amplitude ratio; (c) *Lg/Pg*$_{coda}$ RMS amplitude ratio; (d) time-domain *Lg* coda *Q*. In (a), we see that *Lg* phase is the strongest phase, and can travel to far offset. In (a) and (b), west of the shot, the ratios increase first until~600km, then decrease until ~800km, and then increase again until ~1,200km. They then decrease quite fast; for the right branch, and the ratios increase slowly until ~600km, where they decrease rapidly. Since the Lg phase can only be formed after ~300 km offset, we don't consider the ratio within a 300 km offset. In (d), Lg coda Q is high (~450) for the right branch with offset ~300km – ~600km; Q is lower (~300) at Tunguss basin, and decreases in West-Siberian Basin. (WSB – West Siberian Basin; TB - Tunguss Basin; PVB - Patom-Viluy Basin).

modes. Therefore, it is not clear to what extent the resulting *Lg Q* maps may actually represent spatial gradients of the scattering amplitude.

Scatter in coda *Q* values. Figure 3 shows the logarithm amplitude of Lg coda vs. time for three adjacent traces. The general trend of the three curves is to decrease linearly, but there is local variation, and the local variation for different traces is different. Moreover, there are many low-value spikes in every trace, and there could be data dropouts, and clipping. These problems could seriously contaminate any data analysis results, especially at high-frequencies (Murphy, et el., 2001). So, the local variation of the amplitude and the low-value spikes could be the main reason for the variation of the *Lg* coda *Q*.

Dependence of *Lg* coda *Q* on the time gate and frequency. Figure 3 shows the measured *Lg* coda *Q* values vs. station numbers on the Kimberlite profile for different frequency bands. Despite significant scatter in the values, it is clear that *Lg* coda *Q* increases with frequency. Also, from the figure we can see that a different frequency band has a different response to the variation of the crustal structure. This difference could be a result of the narrow frequency band of the Lg phase.

The discrimination ability of *Lg*(1-2Hz)/*Lg*(6-8Hz). According to Walter et al. (1995), nuclear explosions could be discriminated from earthquakes using spectral ratios *Lg*(1–2Hz)/*Lg*(6–8Hz) or *Lg*$_{coda}$(1–2Hz)/*Lg*(6–8Hz) (Figure 4). For nuclear explosions, these ratios are higher compared to earthquakes, with separation clear above magnitude 3 and increasing with magnitude (Figure 4). Figure 5 shows the *Lg*(1–2Hz)/*Lg*(6–8Hz) RMS amplitude ratio measured from PNEs Craton-3, Kimberlite-3, and Quartz-323. For the PNEs *Lg*(1–2Hz)/*Lg*(6–8Hz) is generally higher than 2, in agreement with the result by Walter et al. (1995).. Also, at offsets of ~500km to ~1,000km, the ratio increases with offset, and thus this could be the best discrimination range.
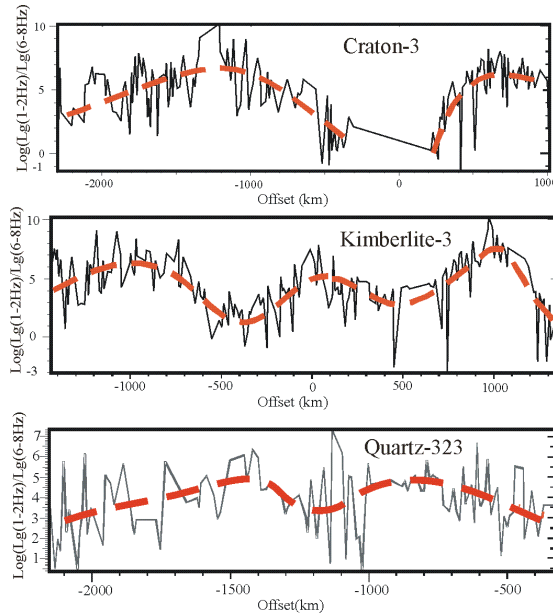

Figure 3. Log(*Lg*(1–2Hz) /*Lg*(6–8Hz) from three PNEs, as labelled. Measured values are shown in the thin black line, and the dashed red line is the interpreted smoothed variations. The log-ratios are usually >2, with significant variations with offset or crustal structure. Near ~1,000 km, the values are generally higher, suggesting that this range could be most efficient for discrimination (see Figure 4).

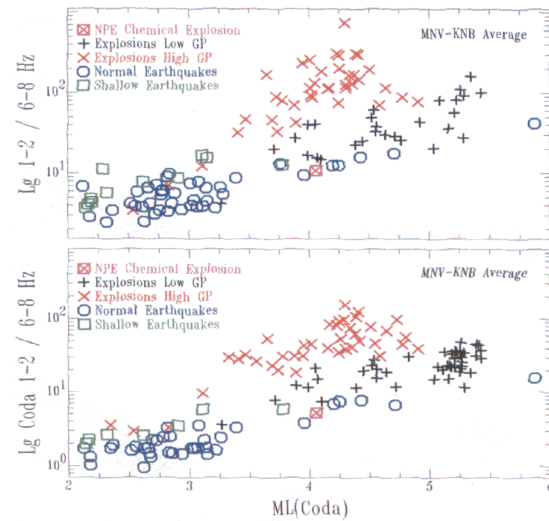**Figure 4. (From Walter et al, 1995) Two-station average (1–2Hz)/(6–8Hz) S wave spectral ratios for (a) *Lg* and (b) *Lg* coda as a function of magnitude. *Lg*(1–2Hz)/*Lg*(6–8Hz) for nuclear explosion is usually higher than from earthquakes with magnitudes >3.**

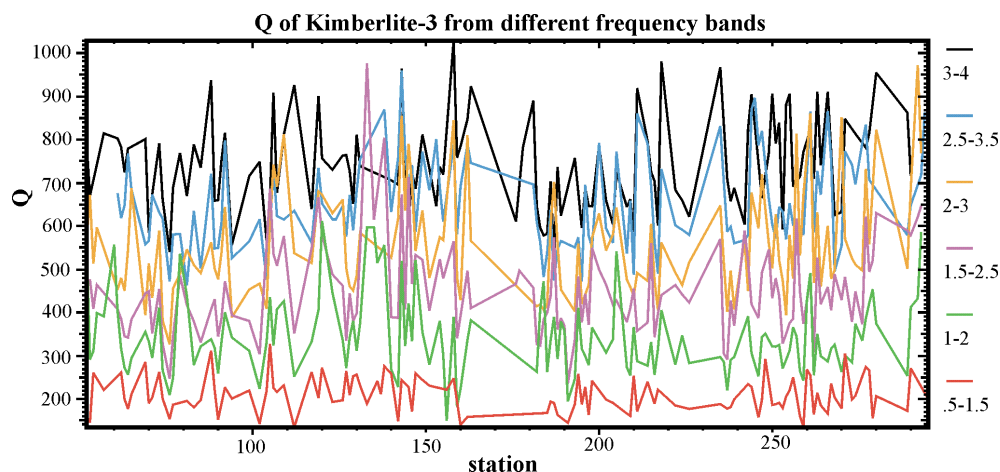**Figure 5.** *Lg* **coda** *Q* **of PNE Kimberlite-3 from in frequency bands (labelled on the right). The** *Lg* **coda** *Q* **increases with frequency. Note that at higher frequencies, the dependence of** *Lg* **coda** *Q* **on frequency decreases.**

Regional variations of *Lg/Sn* **and** *Lg/Pg*$_{coda}$**, and the** *Lg* **coda** *Q* **within the Siberian Craton.** To date, we have analyzed four profiles crossing the Siberian Craton: Craton, Kimberlite, Meteorite, and Rift. Figure 6 shows a summary of the observed characteristics from the four profiles, correlated with the tectonic unites of Northern Eurasia.
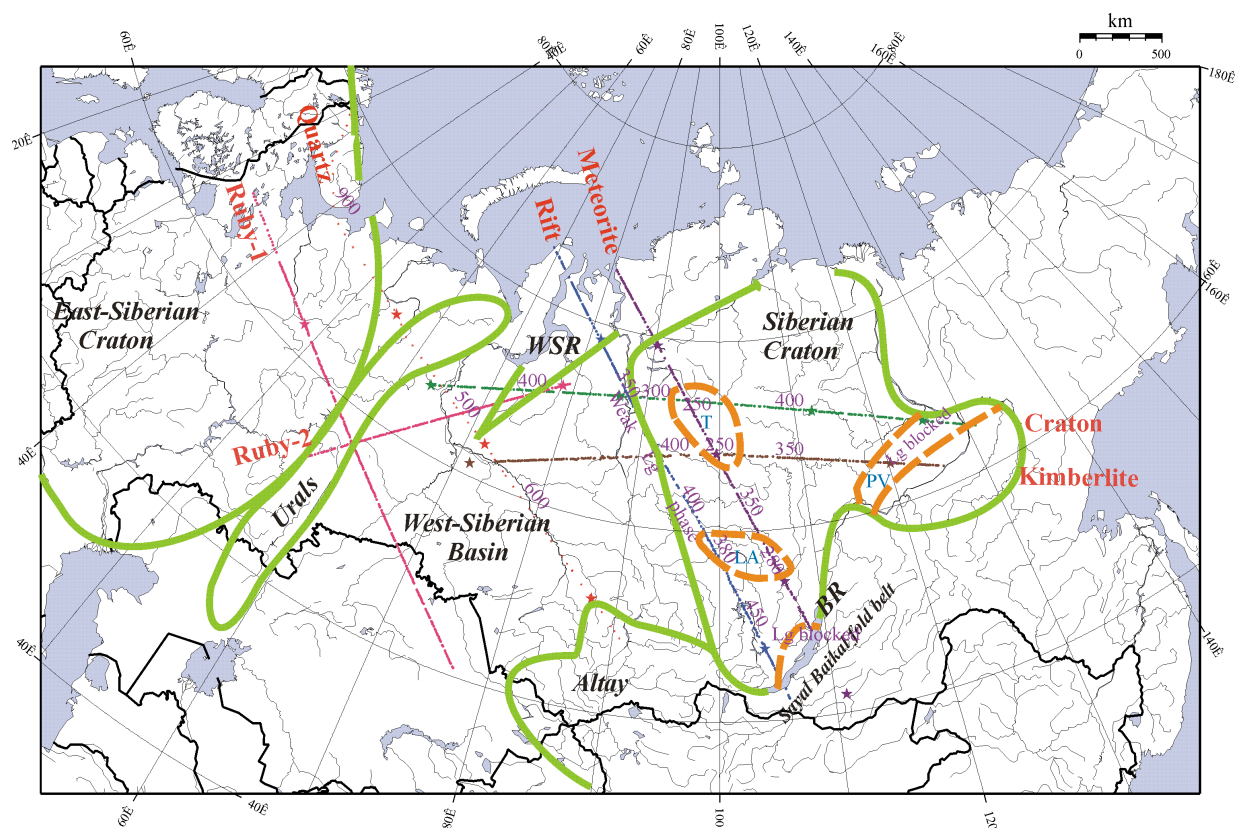

Figure 6. Sketch of the tectonic boundaries of Northern Eurasia (green line), and distribution of the *Lg* **coda** *Q* **and the** *Lg* **phase propagation characteristics. (Green lines show tectonic boundaries, Orange lines indicate areas where** *Lg* **is blocked or highly attenuated areas. WSR indicates the West Siberian Rift, BR – Baikal Rift, T– Tunguss Basin, and PV is the Patom-Viluy basin.**

Numerical coda model. In order to study the relationship between the observed coda Q from the Lg (and also other phases) and the *in situ P*- and *S*-wave crustal Q, we performed numerical simulations of the coda (Duenow, 2003). Morozov and Smithson (2000) argued that for a teleseismic *P*-wave arrival, the coda originates from elliptical areas surrounding the source and receiver, with the upper crust causing most of such scattering. Our scattering model thus represents crustal heterogeneities as scatterers are distributed within the Earth's crust. The resultant scattered coda energy U recorded at a receiver at time t is an integral over scattering volume V:

$$U(\vec{r},t) = \int dt_s \iiint_V d^3\vec{r}_s \Psi(\vec{r}_s) U_{source}(\vec{r}_s,t_s) G(\vec{r}_s,t_s;\vec{r},t), \qquad (3)$$

where t_s is the time of the direct arrival at the scatterer, $\vec{r}_s$ represents scatterer positions, Ψ is the scattering potential describing the amount of energy reflected at the scatterer, and U_{source} is the seismic source function describing energy arriving at the scatterer from the source explosion. G is the scattering from Green's function describing the propagation of scattered energy from scatterer to receiver. For simplicity, because the upper crust is assumed to be the primary contributor to the seismic coda, this volume integral is replaced with a surface integral (Figure 7):

$$U(\vec{r},t) = \int dt_s \iint_S d^2\vec{r}_s \Psi(\vec{r}_s) U_{source}(\vec{r}_s,t_s) G(\vec{r}_s,t_s;\vec{r},t). \qquad (4)$$

The Green's function is approximated as translationally invariant in time and space:

$$G(\vec{r}_s,t_s;\vec{r},t) = G(\vec{r} - \vec{r}_s,t - t_s).$$

Synthetic seismic sections created using the reflectivity method (Fuchs and Müller 1971) were used as source and Green's functions in the model (3-4) (Figure 8).

Note that for a constant scattering potential, the scattering area increases with time after the primary arrival, it will compensate the geometric spreading of the Green's function, and therefore, with no intrinsic attenuation, coda energy would not decay. The observed coda Q was thus thought indicative of the average crustal Q (Morozov and Smithson, 2000).
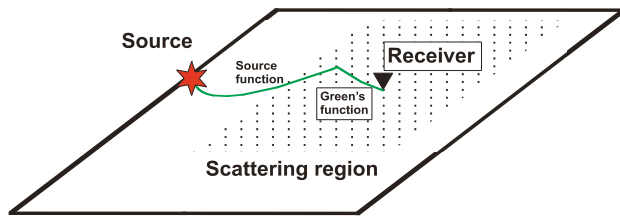

Figure 7. Surface scattering model. Seismic energy originates at source, scatters from uniformly distributed Monte-Carlo-sampled surface points, and is detected at receiver. Source and Green's functions describe propagation of seismic energy.
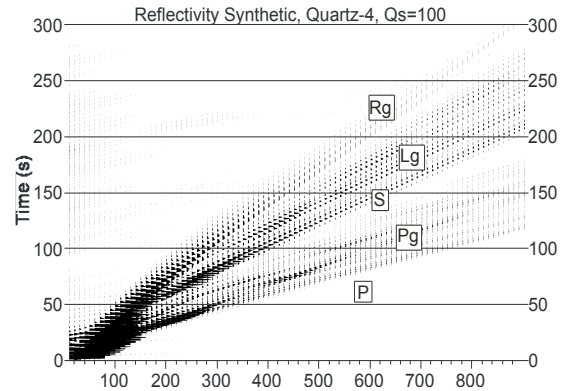

Figure 8. Reflection synthetic seismograms used as the source and Green's functions (Figure 7), created using the Quartz-4 velocity model (Morozova et al., 1999). Note that multiple modes contribute to the scattered coda wavefield.

However, the values of Q_{crust} and Q_{coda} may differ. For example, $Q_{coda} < Q_{crust}$ would indicate that seismic energy is leaking into the mantle and does not return to the surface, whereas. $Q_{coda} > Q_{crust}$ would correspond to mantle phases contributing to the recorded seismic energy. These mechanisms may also be frequency-dependent, causing frequency dependence of the $Q_{coda}(Q_{crust})$ relation.

In our numerical experiments, therefore, we sought an empirical relationship between the observed time-domain log-amplitude coda slope and crustal quality factor:

$$\kappa_{coda} \equiv \frac{f}{Q_{coda}} = \kappa(f)Q_{crust}^{\gamma} , \quad (5)$$

where f is the frequency, κ_{coda} is the observed coda attenuation factor, and $\kappa(f)$ and γ are constants. A power-law relation is used because it is general, asymptotes are well-behaved, and it has been commonly used when determining Q as a function of f in previous studies.

We performed measurements on teleseismic P and L_g codas for four types of velocity models with varying crustal and mantle complexity (of which the preferred the Quartz-4 model, derived using the PNE data; Morozova et al., 1999). Synthetic codas for the Quartz-4 velocity model at $f = 0.3$ Hz are shown in Figure 9. A delay in the onset of coda amplitude is evident between the direct teleseismic P arrival and the strong part of the coda (Figure 9 top and middle) resulting from the low energy of arrivals at the small offset in the Green's functions before the onset of the L_g phase. Since the Green's function is of lower energy at precritical distances (<100–200 km), the coda builds up only after the radius of the scattering ellipse expands beyond this distance.
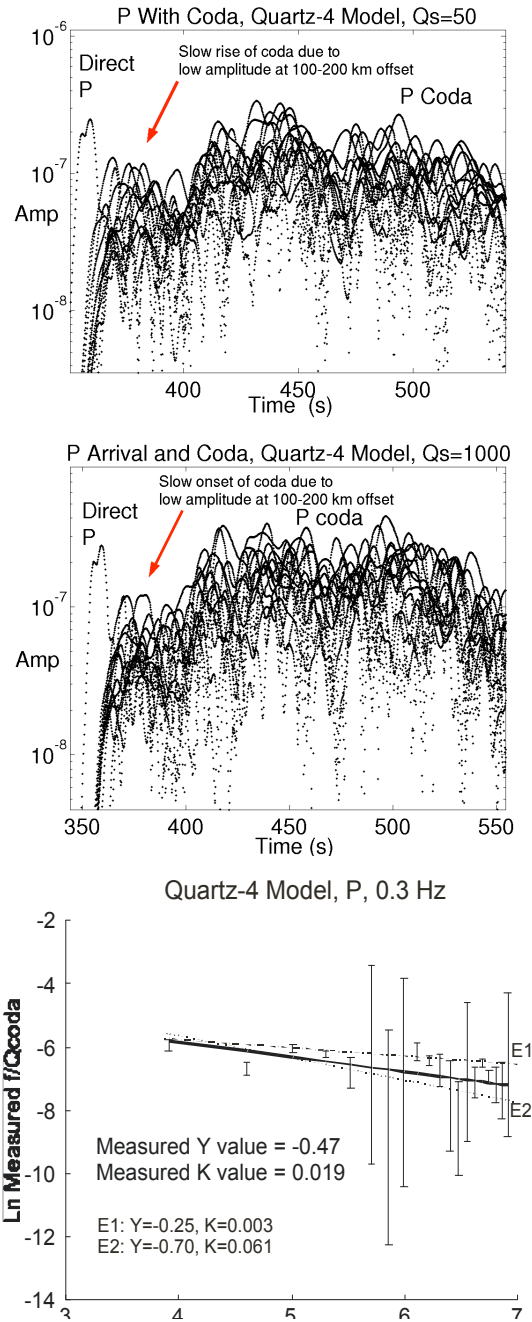
Figure 9. Quartz-4 model results at f=0.3 Hz. *Top and middle:* **Teleseismic *P* direct arrival with coda for**
Q_{crust}=50 and 1000, respectively. Note the noticeably flatter slope for high Q_{crust}. *Bottom*: Slope fitting of
ln(f/Q_{coda}) vs. ln(Q_{crust}) to determine parameters of Q_{coda}-Q_{crust} relation. Note the slow onset of coda energy
after the direct arrival (red arrows).

Synthetics were filtered to center frequencies of 0.3, 0.7, and 1.3 Hz to examine the coda amplitude slopes (5) as a function of frequency. By summarizing the observed measurements (Table 1), we derived an empirical frequency dependence of the parameter k(f) in expression (5).

Estimation of *in-situ* Q_{crust} from *Lg* coda *Q*. Estimates of Q_{crust} for Quartz PNE data were made using the inverse relation of the parameterization (5):

Table 1. Coefficients and exponents of $Q_{coda}(Q_{crust})$ relation. Coefficient is the ratio of f/κ, exponent is $-\gamma$, according to Equation (5).

Model, Coda	0.3 Hz		0.7 Hz		1.3 Hz	
	Coeff.	Exp.	Coeff.	Exp.	Coeff.	Exp.
Quartz-4, P	16	0.47	28	0.43	-	-
IASP-91, P	75	0.06	75	0.14	-	-
IASP-Quartz, P	49	0.14	37	0.42	-	-
Complex Crust, P	2	0.98	25	0.58	-	-
Quartz-4, L_g	18	0.40	63	0.24	65	0.50
Complex Crust, L_g	6	0.78	88	0.22	217	0.07

$$Q_{crust} = \left(\frac{1}{\kappa(f)} \frac{f}{Q_{coda}} \right)^{1/\gamma}, \qquad (6)$$

where f/Q_{coda} is measured from the coda envelope slope, $\kappa(f)$ is determined from a power law (5), and γ is obtained from the parameterization (Table 1). By interpolating the $\kappa(f)$ values (again using a power law) between the imaged points, we obtained an empirical relation mapping the observed Q_{coda} onto crustal Q_{crust} (Figure 10). A surprising observation not well understood at present is the significantly higher P coda Q values as compared to the intrinsic Q of the crust. Apparently the only "physical" explanation of this result is that significant energy propagates through the mantle thereby bypassing the crust (with lower Q) and increasing the overall duration of the coda.

Unfortunately, the modeling program did not allow modeling at high frequencies for the sufficiently long-signal durations necessary to simulate the coda. The primary frequencies of the Quartz data are between 1 Hz and 10 Hz, whereas we were able to model only up to ~2 Hz, and therefore significant extrapolation of the frequency dependencies (5–6) had to be performed. This extrapolation is a major limitation of this approach that may have contributed to the above difficulty and will need to be overcome in the future.

By using the P-wave coda measurements by Morozov and Smithson (2000), combined with several additional frequency points, we obtained revised crustal Q estimates (Figure 11). Crustal Q values increase with frequency, as suggested by Morozov and Smithson (2000); however the resulting values of Q_{crust} are somewhat surprisingly low, ranging between ~60–150. Such low values arise from the anomalously high-modeled coda Q value mentioned above.
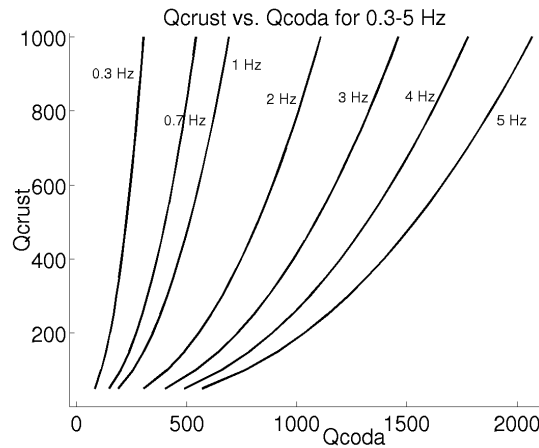
Figure 10. Empirical inverse $Q_{crust}(Q_{coda}, f)$ dependence of Quartz-4 model derived for *P*-wave coda from our numerical simulations.
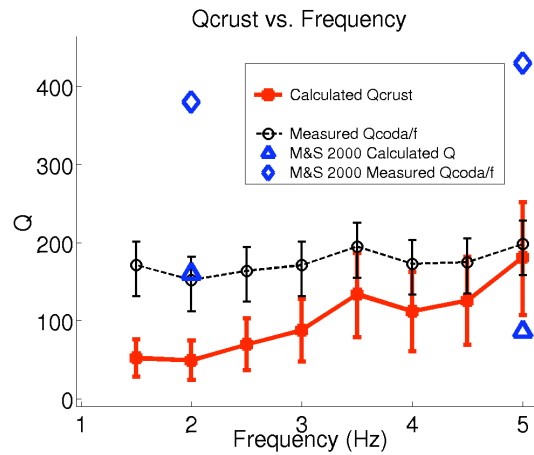

Figure 11. *Q* values as a function of frequency, from Quartz-323 coda measurements. Circles with black line are measured Q_{coda}/f values. Error bars were chosen as 30 above and 40 below the measured value. Squares with red line are the Q_{crust} values computed using Equation (6) to determine relation as a function of frequency. Q_{crust} values appear to generally increase with increasing frequency. Error bars are propagated from those on the Q_{coda}/f values. For comparison, blue triangles at 2 Hz and 5 Hz represent values of Q_{coda}/f by Morozov and Smithson (2000), with corresponding estimates of Q_{crust} shown by blue diamonds.

CONCLUSIONS AND RECOMMENDATIONS

Lg/Sn and Lg/Pg_{coda} amplitude ratios show significant correlation with crustal thickness; in particular, these ratios decrease sharply within thick sedimentary basins. The Lg coda Q appears to correlate with tectonic types, but also with the variations of the crustal structures, such as the sediment and crustal thickness. The two effects are not easy to differentiate, because deep basins are usually associated with shallowing Moho resulting from isostatic effects.

In the Siberian Craton, the Lg coda Q is highly variable. The attenuation is much higher (Q is ~280–350) within the deep sedimentary basins, and Q ≈400–450 in areas with thinner sedimentary covers.

Lg(1–2Hz)/Lg(6–8Hz) ratios measured using DSS PNE records fall within the explosion population. Variation of these ratios with offsets suggest that distances of ~1,000 km could be the best used as the discriminant in Northern Eurasia.

Numerical modeling of the P- and Lg-arrival coda from PNEs suggests that the observed coda Q may be higher than the intrinsic Q of the crust. This difference could be because of the contribution of mantle-guided phases into the coda. As a consequence of this result, the crustal Q values may be overestimated when judged by the observed Lg coda Q.

Teleseismic P Q_{coda} values measured from the envelope of a set of Quartz PNE traces gave Q_{crust} values of 50 at 2 Hz, increasing to 175 at 5 Hz, for the East European Platform. These crustal values are commensurate with others obtained previously in other regions. The Quartz-4 L_g parameterization at 1.3 Hz gave a Q_{crust} estimate of 21 for the West Siberian Basin using the PNE Quartz L_g coda, which we expected to be lower since the trace was recorded in a region of thick sediments.

REFERENCES

Campillo, M., and J. L. Plantet (1991). Frequency dependence and spatial distribution of seismic attenuation in France: experimental results and possible interpretations. Physics of the Earth & Planetary Interiors, 67: 48-64.

Duenow, J. N. (2003). Surface Scattering as a Source of Teleseismic Arrival Coda, M.S. thesis., University of Wyoming, Laramie, WY.

Mitchell, B. J., Y. Pan, J. Xie, and L. Cong (1997) Lg coda Q variation across Eurasia and its relation to crustal evolution. Journal of Geophysical Research, 102(B10): 22767-22779.

Mooney, W.D. (2002). Crustal and upper mantle seismic velocity structure of the former USSR. 21st Seismic Research Symposium, 162-171.

Morozov, I.B. and Smithson, S.B., 2000. Coda of Long-Range Arrivals from Nuclear Explosions, Bull. Seis. Soc. Am. 90, 929-939.

Morozova, E.A., I. B. Morozov, S. B. Smithson, and L. N. Solodilov (1999). Heterogeneity of the uppermost mantle beneath Russian Eurasia from the ultra-long profile QUARTZ, J. Geophys. Res. 104, no. B9, 20329-20348.

Murphy, J.R., I. O. Kitov, B. W. Barker, and D. D. Sultanov (2001). Seismic source characteristics of Soviet peaceful nuclear explosions. Pure and Applied Geophysics, 158: 2077-2101.

Pavlenkova, N.I. (1996). Crust and upper mantle structure in Northern Eurasia from seismic data. Advances in Geophysics, 37: 1-333.

Pavlenkova, G.A., K. Priestley, and J. Cipar (2002). 2D model of the crust and uppermost mantle along rift profile, Siberian Craton. Tectonophysics, 355: 171-186.

Sandvol, E., K. Al-Damegh., A. Calvert, D. Seber,M. Barazangi, R. Mohamad, R. Gök, N. Türkelli, and C. Gürbüz (2001). Tomographic imaging of Lg and Sn propagation in the Middle East. Pure and Applied Geophysics, 158: 1121-1163.

Walter, W.R.,K. M. Mayeda, and H. J. Patton (1995). Phase and spectral ratio discrimination between NTS earthquakes and explosions. Part I: empirical observations. Bulletin of the Seismological Society of Americas, 85: 1050-1067.

Zonenshain L.P., M. I. Kuzmin, and B. M. Natapov (1990). Geology of the USSR: a plate tectonic synthesis. American Geophysical Union, Washington, D.C.